https://doi.org/10.5194/egusphere-2025-6285
Preprint. Discussion started: 5 January 2026

Impact, drivers and pathways of two Arctic atmospheric rivers in April 2020

Luisa E. Avilés-Podgurski[1,2], Patrick Martineau[3], Hua Lu[1], Ayako Yamamoto[4], Amanda C. Maycock[2], Andrew Orr[1], Tony Phillips[1], Thomas J. Bracegirdle[1], Anna E. Hogg[2], Grzegorz Muszynski[5], and Andrew Fleming[1]

[1]British Antarctic Survey, Cambridge, UK.
[2]School of Earth and Environment, University of Leeds, Leeds, UK.
[3]Application Laboratory, Japan Agency for Marine-Earth Science and Technology, Yokohama, Japan.
[4]College of Arts and Sciences, J. F. Oberlin University, Tokyo, Japan.
[5]School of Geosciences, University of Edinburgh, Edinburgh, UK.

Correspondence: Luisa E. Avilés-Podgurski (luiile20@bas.ac.uk)

Abstract. Atmospheric rivers (ARs) play a major role in transporting heat and moisture into the Arctic, yet their thermodynamic structure and regional impacts remain poorly understood. Here, we adopt a combined Eulerian-Lagrangian framework to investigate two intense ARs that penetrated into the central Arctic within one week in April 2020, providing a comprehensive view of their large-scale dynamics, moisture sources, and thermodynamic evolution.

The first AR entered the Arctic via the Siberian sector, driven by a highly anomalous quasi-stationary anticyclone over north-central Siberia. The second followed an Atlantic pathway and was associated with an unusually deep and persistent cyclone over Baffin Bay. Despite their distinct origins and pathways, both events produced extreme surface impacts, including widespread warming across Eurasia exceeding 9°C over a 7-day period and intense precipitation along the Greenland coast and in the central Arctic. The events coincided with a notable decline in sea ice extent in the Barents-Kara Sea and along eastern Greenland, that is highly correlated with the AR-induced warming and rainfall.

Backward trajectory analysis of air parcels associated with extreme Arctic precipitation reveals distinct pathways and thermodynamic evolution. One group of parcels associated with overall cooling and increases in potential temperature exhibits classic AR characteristics: warm, moist, low-pressure airmasses that ascended upon arrival and released intense precipitation. Moisture sources however differed by pathway: the Atlantic AR drew from the warm Gulf Stream region, while the Siberian AR was fed by continental Eurasia. These findings highlight the diverse origins and mechanisms of ARs and their capacity to drive rapid Arctic climate and cryospheric changes.

1 Introduction

Atmospheric rivers (ARs) are narrow bands of enhanced water vapour that play a crucial role in transporting moisture into the Arctic (Doyle et al., 2011; Liu and Barnes, 2015; Papritz et al., 2022). ARs primarily originate in the subtropics and mid-latitudes (Guan and Waliser, 2015) and are steered poleward by synoptic weather systems commonly associated with strong

https://doi.org/10.5194/egusphere-2025-6285
Preprint. Discussion started: 5 January 2026

low–high pressure couplets (Dacre et al., 2015; Wang et al., 2024). Despite their episodic nature, ARs account for over 90% of the total poleward moisture transport through the midlatitudes, making them key actors in the global hydroclimate (Zhu and Newell, 1998; Nash et al., 2018).

Recent decades have seen a rise in AR frequency in the Arctic (Zhang et al., 2023; Wang et al., 2024; Gong et al., 2025; Thaker et al., 2025). Such Arctic ARs occur year-round, following seasonally-dependent pathways that are mostly concentrated over water bodies, where continuous evaporation provides the necessary moisture supply (Salimi et al., 2020; Pan et al., 2024). Important AR pathways into the Arctic include the Pacific sector and the North Atlantic (Nash et al., 2018; Gong et al., 2025; Tiedeck and Rinke, 2025), particularly in association with cyclones forming and deepening near Greenland (Papritz et al., 2022; Loeb et al., 2024). The observed increase in Arctic AR occurrences is in line with projections under climate change indicating a poleward shift of more frequent and intense ARs (Payne et al., 2020). Concurrently, the Arctic is undergoing accelerated surface warming, a phenomenon known as Arctic amplification (Serreze and Barry, 2011; Previdi et al., 2021). Enhanced poleward moisture transport has emerged as a key driver of this amplification, suggesting that continued increases in AR activity may exacerbate stress on an already vulnerable system (Doyle et al., 2011; Neff, 2018; Hao et al., 2019).

ARs can induce surface warming in the Arctic through various physical mechanisms. The greenhouse effect of water vapour, and the latent heat released during condensation in advected airmasses can cause significant warming and promote surface melt (Boisvert et al., 2016; Mattingly et al., 2018). Increased atmospheric moisture also leads to the formation of extensive cloud bands with high liquid water content, which enhance downwelling longwave radiation and sensible heat fluxes (Svensson et al., 2023; Li et al., 2024). This additional thermodynamic forcing contributes to surface warming, while simultaneously reducing the efficiency of the Arctic surface to cool radiatively (Doyle et al., 2011; Graversen et al., 2011; Cullather et al., 2016; Hegyi and Taylor, 2018). AR-induced rain-on-snow events and melt further reduce the surface albedo, amplifying surface warming (Zhang et al., 2023; Kolbe et al., 2025). Lastly, as an AR is advected into the polar environment, the warm, moist air is forced upward by the cold Arctic air, leading to a combination of condensation, cloud formation, and precipitation accompanied by further latent heat release (Komatsu et al., 2018).

ARs are increasingly recognized as a major driver of sea ice variability in the Arctic, capable of both inhibiting growth and inducing loss (Hegyi and Taylor, 2018; Zhang et al., 2023; Gong et al., 2025; Thaker et al., 2025; Zhang et al., 2025). For instance, during the 2016-2017 winter season, ARs contributed to a record-low sea ice extent and substantial thinning (Binder et al., 2017; Hegyi and Taylor, 2018). In 2012 and 2020, years characterised by extremely low summer sea ice extent, individual ARs drove rapid and substantial sea ice loss (Li et al., 2024). While Li et al. (2024) highlight the dominant role of turbulent heat fluxes and strong near-surface winds that promote sea ice advection and rapid retreat along the sea ice margins, other studies identify enhanced downwelling longwave radiation as a key driver of AR-induced sea ice decline (Doyle et al., 2011; Graversen et al., 2011; Cullather et al., 2016; Hegyi and Taylor, 2018).

https://doi.org/10.5194/egusphere-2025-6285
Preprint. Discussion started: 5 January 2026

ARs also exert substantial impacts on the Greenland Ice Sheet by modulating surface energy and mass balance through moisture transport, melt processes, and snowfall (Bonne et al., 2015; Neff, 2018; Box et al., 2022; Loeb et al., 2024). Anomalously high moisture transported by ARs has been linked to enhanced surface melting and substantial mass loss (Mattingly et al., 2018). Landfalling ARs can also trigger föhn winds that drive exceptional melt episodes and speed-ups of outlet glaciers, whereas heavy snowfall during some AR events can increase the surface mass balance (Neff, 2018; Mattingly et al., 2023). Collectively, these studies underscore the role of ARs as episodic but potent drivers of cryosphere disruption and Arctic climate variability (Mattingly et al., 2023).

Two distinct ARs travelled along different pathways before intruding into the Arctic during 13-21 April 2020. One AR travelled from northwestern Russia, while the second propagated poleward from the northern Atlantic (Kirbus et al., 2023). Both ARs reached the central Arctic, where their presence led to unprecedented high moisture and suppressed outgoing longwave radiation together with a stark 30°C surface warming that resulted in record-breaking daily temperatures (Rinke et al., 2021). The ARs coincided with the Multidisciplinary Drifting Observatory for the Study of Arctic Climate (MOSAiC) expedition (Nicolaus et al., 2022; Shupe et al., 2022), passing directly above the the research vessel (RV) *Polarstern*, thus providing unique in-situ measurements from ship and the surrounding sea ice.

Previous studies have examined this episode from different perspectives. Kirbus et al. (2023) examined the poleward latent energy transport across the Arctic Circle and investigated the cloud and moisture properties around RV *Polarstern*. Dada et al. (2022) focused on aerosol transport and transformations near the ship. Svensson et al. (2023) investigated warm-air intrusions using MOSAiC data with a focus on airmass transformation, vertical structure, and surface energy exchanges.

Given the significant impacts that these ARs exerted on the Arctic, a deeper understanding of their origins, pathways, and poleward moisture transport is essential. Moreover, key questions remain regarding how unusual the synoptic-scale drivers were that contributed to the extremeness of the two ARs, how the ARs are linked to surface impacts and sea ice loss beyond the immediate MOSAiC site, and how they evolved thermodynamically along their pathways. Our study addresses this gap by combining Eulerian and Lagrangian perspectives to trace the AR airmass origins, transport pathways, and thermodynamic changes. This broader approach complements previous work and provides new insights into AR dynamics and impacts during an unprecedented event.

2 Data and Methods

We employ a number of different tools to study the two ARs that reached the Arctic in April 2020. The AR originating from northwestern Russia is referred to as the *Siberian AR*, while the AR originating from the North Atlantic is termed the *Atlantic AR*. We further define 15–21 April 2020 as the *target period*, during which both ARs were located within the Arctic Circle (north of 66.34°N).

https://doi.org/10.5194/egusphere-2025-6285
Preprint. Discussion started: 5 January 2026

2.1 ERA5 reanalysis data

We use the European Centre for Medium-range Weather Forecasts (ECMWF) fifth generation reanalysis data set ERA5 (Hersbach et al., 2020) to analyse meteorological fields linked to the two Arctic ARs. Daily mean sea level pressure (MSLP), 2-m surface temperature (T2m), precipitation, and rainfall data at $0.25° \times 0.25°$ horizontal grid spacing are used. Anomalies are calculated as deviations from the April mean climatology for the period 1979–2023. Daily T2m anomalies are further averaged over the target period to quantify the longer-lasting impact of the ARs on surface temperature. In addition, daily T2m, precipitation and rainfall data are used to compute time series over distinct regions in the Arctic where the largest changes in sea ice concentration are observed associated with the ARs.

To assess how unusual the low- and high-pressure systems associated with the Arctic ARs were with respect to the 1979-2023 period, we determine the 7-day averaged MSLP anomaly field for the target period and define boxes enclosing each weather system. For each box, a reference distribution of 7-day mean MSLP anomalies is constructed for April 1979–2023 using a 7-day moving window. The percentile of the target period anomaly is then computed within this distribution.
A similar approach is applied to T2m. 7-day mean T2m anomalies for April 1979-2023 are spatially averaged over regions within the Arctic Circle (north of $66.34°$N) where the ARs prevailed for at least three days, forming a reference distribution. The percentile of the target period T2m anomaly is then calculated relative to this distribution. For precipitation, we compute 7-day accumulated precipitation amounts at each grid cell for April 1979-2023. The value for the target period at each grid cell is then compared against the corresponding reference distribution.

2.2 Sea ice data

To derive sea ice extent and sea ice concentration (SIC) changes, we use the daily sea ice concentration product OSI-401-b produced by the EUMETSAT Ocean and Sea Ice Satellite Application Facility (OSI SAF) at a 10 km horizontal resolution (Tonboe and Lavelle, 2016). The global SIC data is derived from atmospherically corrected passive microwave satellite (SSMIS) brightness temperatures over the polar regions using the OSI SAF algorithm. Sea ice extent is defined based on a 15% threshold of SIC.

2.3 Observational data from MOSAiC

To investigate the local meteorological conditions around RV *Polarstern* associated with the two Arctic ARs, we analyse high-resolution in-situ observations from the MOSAiC expedition, a year-long, icebreaker-based research mission that took place from September 2019 to October 2020 (Shupe et al., 2020). During this period, the RV *Polarstern* drifted with the sea ice across the central Arctic Ocean, providing an unprecedented opportunity to observe air–surface interactions in the high Arctic.

We use processed and quality-controlled Level 3 data with 10-minute temporal resolution for T2m, 2-m specific humidity (Q2m), and surface energy balance (SEB) components aggregated to 6 hours. The SEB components include incoming (in) and

https://doi.org/10.5194/egusphere-2025-6285
Preprint. Discussion started: 5 January 2026

outgoing (out) shortwave (SW) and longwave (LW) radiation, as well as latent heat (LH) and sensible heat (SH) fluxes. The SEB is computed as

$$SEB = SW_{in} - SW_{out} + LW_{in} - LW_{out} + LH + SH,$$

so that SEB is positive when incoming exceed outgoing fluxes.

These measurements were collected at the 'Met City' observation site located on the sea ice near *Polarstern*, which was equipped with a 10-metre micrometeorological tower, a 23–30 metre telescoping mast, and a radiation station (Cox et al., 2023). In addition, we use precipitation measurements at 1-minute time intervals from a vertically-pointing ka-band radar mounted on the ship accumulated to 6-hourly data. Together, these observations provide a detailed view of the thermodynamic and radiative processes during AR intrusions into the central Arctic.

2.4 AR detection

To study the two Arctic ARs, we use the global AR database produced by Guan and Waliser (2024). This dataset is based on version 4 of the Tracking Atmospheric Rivers Globally as Elongated Targets (tARget) algorithm applied to ERA5 reanalysis data for 1940–2023 at 6-hour intervals and a horizontal grid spacing of $0.25° \times 0.25°$.

tARget identifies AR objects based on integrated water vapour transport (IVT), geometry requirements and direction of motion (Guan and Waliser, 2015, 2024). It employs a hybrid thresholding approach that combines a month- and location-dependent 85th percentile IVT threshold with a hemispherically fixed, month-dependent threshold derived from the area-weighted spatial 5th percentile for each hemisphere. This combination enhances AR detection in regions where IVT is climatologically low, such as the cold and/or dry Arctic. Additionally, the tARget algorithm is capable of tracking ARs through space and time following its life cycle and extracting key characteristics such as life time, travel distance and mean zonal and meridional IVT, all of which are included in the global AR database.

2.5 Lagrangian parcel tracking

To investigate the thermodynamic evolution of airmasses and the moisture budget associated with the two Arctic ARs, we use the Lagrangian Analysis Tool LAGRANTO v2.0 (Sprenger and Wernli, 2015). Parcels are initialised at 80 hPa vertical intervals between 1000 and 200 hPa on an equidistant 100 km grid within the AR boundaries defined by the global AR database (Guan and Waliser, 2024). Parcels are released every 6 hours for the period 13–21 April 2020 and tracked backward in time for 9 days. The trajectory calculations use the three-dimensional wind field and pressure retrieved from hourly ERA5 reanalysis data with a horizontal grid spacing of $0.5° \times 0.5°$. Along each trajectory, temperature, pressure (p), and specific humidity (Q) are traced. Additionally, potential temperature (θ) and temporal changes of pressure (dp/dt) and specific humidity (dQ/dt) are

https://doi.org/10.5194/egusphere-2025-6285
Preprint. Discussion started: 5 January 2026

computed to identify vertical motion and moisture exchange processes.

To identify the parcel trajectories relevant to extreme Arctic precipitation associated with the two ARs, we retain only those with endpoints within the Arctic Circle along the Greenland coast and in the central Arctic, where 7-day accumulated precipitation exceeds the 90th percentile (white stippling in 5a). As only the Atlantic AR contributes to precipitation along the Greenland coast, we perform separate analyses for the respective two regions. Instead of keeping a uniform trajectory length of 9 days across all parcel trajectories, the trajectory length is optimised for each region to best capture the thermodynamic evolution of air parcels most closely associated with ARs, accounting for both AR lifetime and the temporal variability of key thermodynamic parameters. Sensitivity analyses confirm that the results remain qualitatively consistent for trajectory lengths within the typical range of 5–9 days (not shown).

Following Binder et al. (2017), we identify the maximum difference in temperature (ΔT) and potential temperature ($\Delta\theta$) along each trajectory relative to their endpoint values, effectively grouping the parcels into four subcategories. This approach provides insight into the adiabatic and diabatic processes experienced by the air parcels: trajectories with positive (negative) ΔT indicate a net temperature increase (decrease), while those with positive (negative) $\Delta\theta$ primarily reflect diabatic heating (cooling). This classification thus distinguishes airstreams with distinct thermodynamic characteristics.

3 Results

3.1 Synoptic drivers of the Siberian and Atlantic ARs

Fig. 1 shows that the Siberian and Atlantic ARs, each steered by a cyclone–anticyclone couplet, followed distinct pathways before merging in the central Arctic. Both reached RV *Polarstern* within a few days. The first AR, the Siberian AR, advances into the Arctic Circle on 13 April 2020 after travelling across Europe and Scandinavia, defining what we term the *Siberian pathway*. It is steered by a quasi-stationary anticyclone over Siberia, located east of the AR, which deepens between 16–18 April. On the western flank of the AR, the associated cyclone lies over Scandinavia on 13–14 April. It then strengthens and shifts eastward by 16 April, displacing the AR further east. The second AR, the Atlantic AR, propagates northward along the Atlantic Ocean and reaches the Arctic Circle three days after the Siberian AR on 16 April. The associated quasi-stationary cyclone develops over Baffin Bay west of Greenland, a region where cyclones frequently become occluded and slow-moving (Bintanja and Selten, 2014; Loeb et al., 2024). Together with a persistent anticyclone over the UK, the cyclone-anticyclone couplet steers the Atlantic AR towards south-eastern Greenland on 16-17 April. This coincides with the region of Greenland with the highest frequency of landfalling ARs (Waling et al., 2024). The cyclone undergoes rapid deepening and expands on 17 April while the anticyclone strengthens over Scandinavia, steering the AR further through the Fram Strait into the central Arctic. After the two ARs merge in the central Arctic on 19 April, residual AR airmasses persist until 21 April, sustained by anomalous low pressure north and north-west of Greenland and by two anticyclones, one over central–eastern Siberia and the

https://doi.org/10.5194/egusphere-2025-6285
Preprint. Discussion started: 5 January 2026

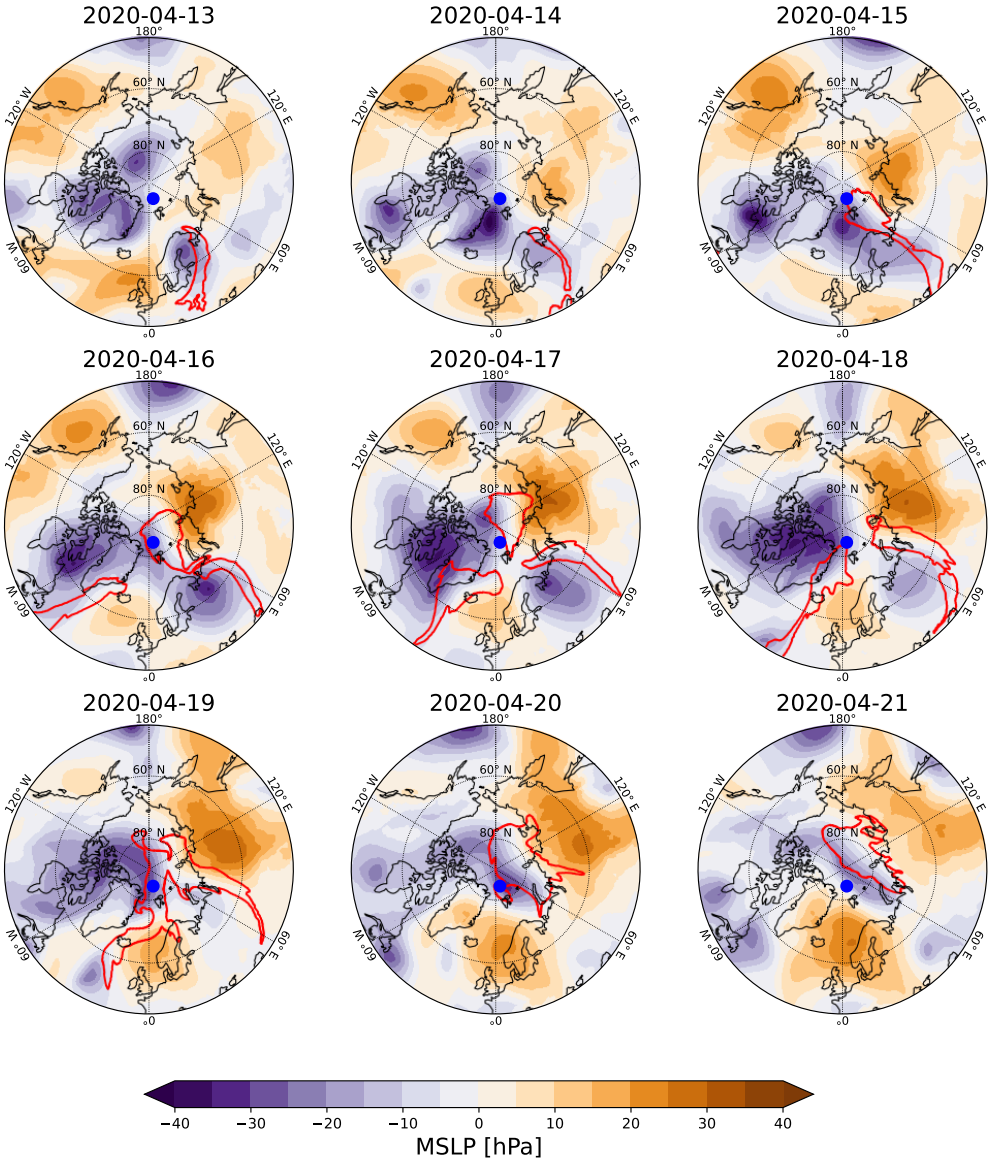

Figure 1. Synoptic conditions based on ERA5. MSLP anomalies relative to the April climatology (shading) are shown for each day for 13-21 April 2020. Red contours outline the shapes of the Atlantic and Siberian ARs at 12:00 UTC of the respective days diagnosed from the tARget database. The position of RV *Polarstern* is indicated by the blue dot.

https://doi.org/10.5194/egusphere-2025-6285
Preprint. Discussion started: 5 January 2026

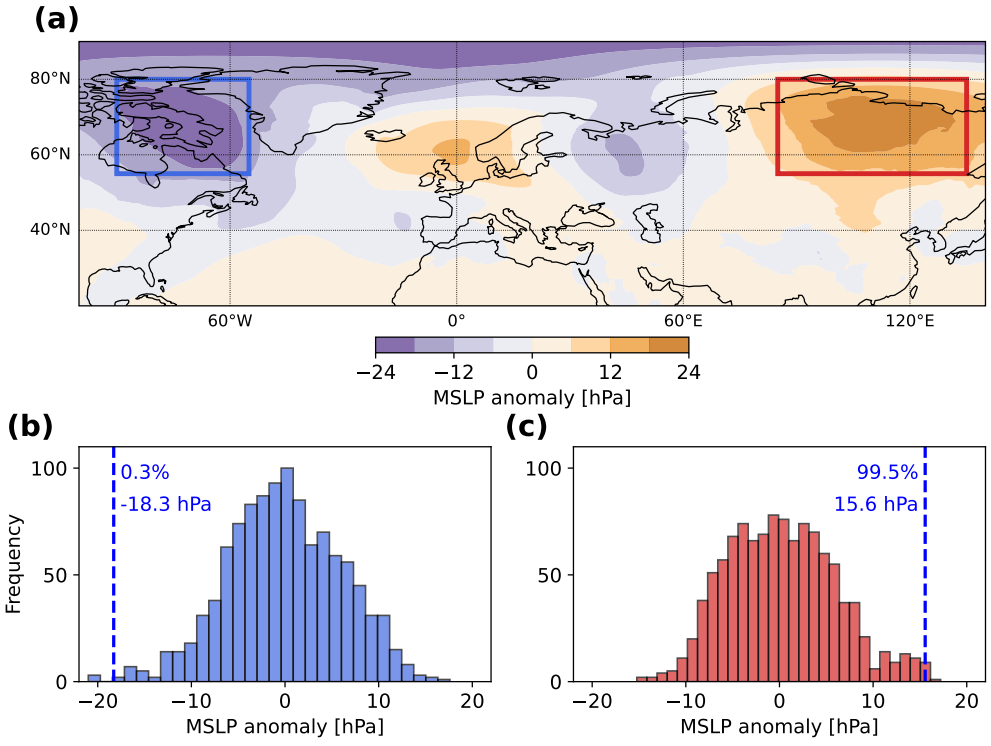

Figure 2. Assessing the extremeness of the synoptic weather systems driving the Atlantic and Siberian ARs based on ERA5. (a) 7-day mean MSLP anomalies for 15-21 April 2020 relative to the April climatology. The extratropical cyclone west of Greenland is enclosed by a blue box (55°–90°W and 55°–80°N) while the anticyclone over northern Siberia is marked by a red box (85°–135°E and 55°–80°N). (b) Distribution of 7-day mean MSLP anomalies spatially averaged over the blue box in (a) for April 1979-2023. The anomaly of the target period is indicated by a blue vertical line, annotated with the percentile and mean anomaly. (c) As (b) but for the region enclosed by the red box in (a).

other over Scandinavia.

To further investigate how unusual the persistent large-scale weather systems were that steered the Atlantic and Siberian ARs into the Arctic, the 7-day averaged MSLP anomaly for the target period is computed. Figure 2a reveals a wave train of alternating high- and low-pressure systems across the mid- to high latitudes. This pattern features a deep cyclone over Baffin Bay, an anticyclone over the northeastern Atlantic, a cyclone over western Russia, and a pronounced anticyclone over northern Siberia, with each cyclone-anticyclone couplet steering one of the two ARs poleward. The cyclone centred over Baffin Bay (blue box) exhibits an exceptional 7-day mean anomaly of $-18.3\,\mathrm{hPa}$, placing it in the lowest 0.3% of the climatological distribution for 1979-2023 over the same region (Fig. 2b), highlighting the rarity of such a persistent and strong negative MSLP anomaly over Baffin Bay. The accompanying anticyclone over the northern Atlantic is characterised by a 7-day mean anomaly

https://doi.org/10.5194/egusphere-2025-6285
Preprint. Discussion started: 5 January 2026

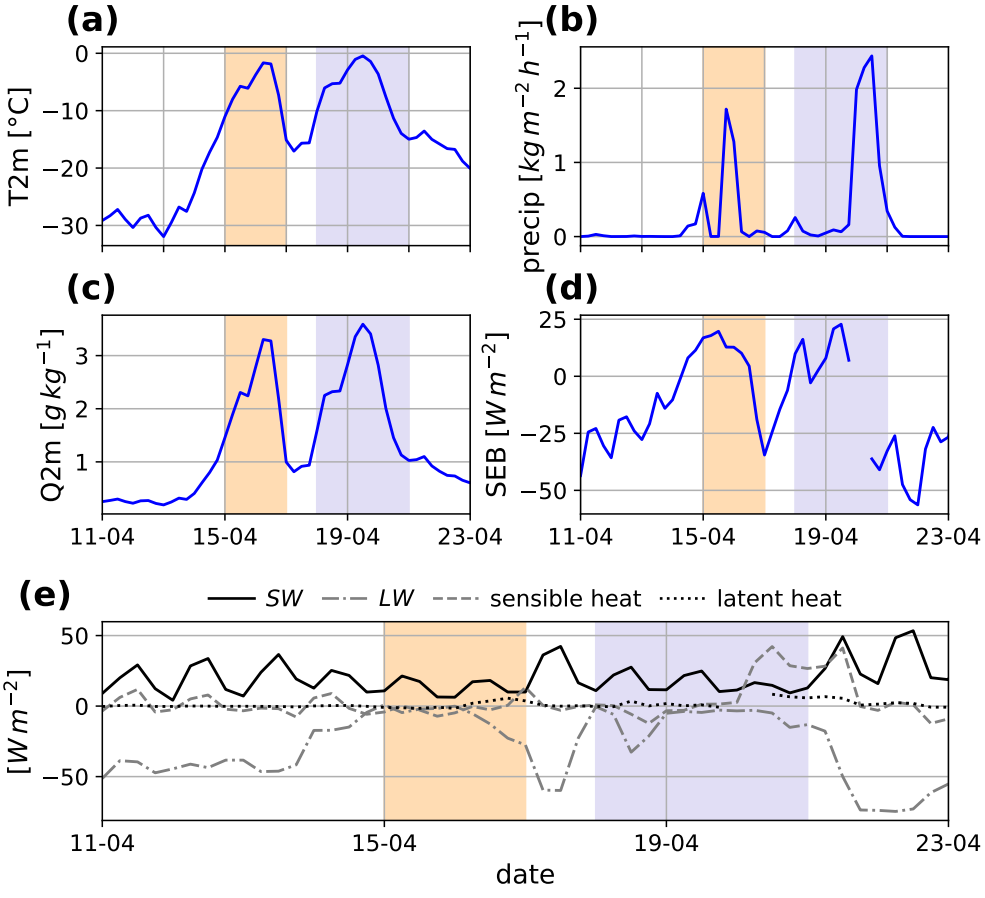

Figure 3. In-situ observations from MOSAiC for 11-23 April 2020. Shown are time series of (a) T2m, (b) total precipitation, (c) Q2m, (d) SEB, and (e) individual SEB components including radiative and turbulent surface fluxes. SW (LW) denotes the net shortwave (longwave) flux, defined as the difference between incoming and outgoing radiation. Shaded areas indicate periods when the Siberian AR (orange) and the Atlantic AR (purple) were located over the research vessel.

of 6.6 hPa, corresponding to the upper 86.1% of its distribution (not shown). Meanwhile, the cyclone centred over western Russia forming part of the cyclone-anticyclone couplet associated with the Siberian AR, is characterised by a 7-day mean of −7 hPa, placing it at the lower 11.6% of its distribution (not shown). The anticyclone over northern Siberia (red box), in contrast, is highly anomalous with a 7-day mean anomaly of 15.6 hPa placing it in the upper 99.5% of the distribution (Fig. 2c). The corresponding distribution is non-Gaussian, with a bell-shaped core from –10 to +10 hPa and a pronounced heavy tail toward positive values.

https://doi.org/10.5194/egusphere-2025-6285
Preprint. Discussion started: 5 January 2026

3.2 MOSAiC in-situ observations

Next, we examine the impact of the Siberian and Atlantic ARs on surface conditions near RV *Polarstern* (Fig. 3). The arrival of the Siberian AR is marked by a stark rise in T2m (Fig. 3a), increasing from about -30°C on 13 April to just below 0°C on 16 April. This warming is accompanied by a pronounced increase of roughly 3 $\mathrm{g\,kg^{-1}}$ in Q2m (Fig. 3c) and a steady increase in SEB (Fig. 3d) from negative to positive values. Positive SEB values persist for about 2 days, indicating a net transfer of energy from the atmosphere to the surface and suggesting surface melt. Consistent with previous studies (e.g., Cullather et al., 2016), the increase in SEB under AR conditions is primarily driven by enhanced net longwave radiation, while turbulent fluxes play a comparatively minor role (Fig. 3e). A spike in total precipitation occurs while the Siberian AR remains above the ship on 16 April (Fig. 3b), coinciding with a sharp decline in Q2m and SEB. By 17 April, both variables return to values similar to those before the AR event, suggesting a transition to clear-sky conditions. T2m also drops rapidly by about 15°C between 16-17 April, while still remaining well above pre-Siberian AR temperatures.

The Atlantic AR reaches RV *Polarstern* on 18 April, marking the onset of a rise in T2m (Fig. 3a) and Q2m (Fig. 3c). Both peak at even higher values than during the Siberian AR, with T2m slightly surpassing 0°C. SEB (Fig. 3d) also increases to high positive values, reflecting enhanced energy influx to the surface. Between 19-21 April, precipitation (Fig. 3b) reaches amounts approximately 2.5 times greater than those during the Siberian AR. Data gaps in SEB coincide with the period of intense precipitation. Analysis of the individual SEB components (Fig. 3e) again shows that the increase in SEB is primarily driven by enhanced longwave radiation directed towards the surface, likely associated with increased cloud cover, whereas turbulent fluxes contribute only marginally. After the retreat of the Atlantic AR, Q2m and SEB return to levels similar to those before the Siberian AR. T2m decreases gradually to around -20°C but does not decrease to pre-AR temperatures, marking the transition from winter to spring (Svensson et al., 2023).

3.3 Impact on surface temperature, precipitation and sea ice

After having analysed the synoptic-scale context of the two ARs and their impacts on surface conditions around RV *Polarstern*, we examine how the two ARs impacted T2m, precipitation and sea ice extent in the wider Arctic. Strong positive T2m anomalies averaged over the target period 15-21 April 2020 are shown in Fig. 4a with anomalies exceeding 6°C located over Greenland, central Siberia and the central Arctic. Further, widespread positive T2m anomalies of 3-9°C dominate central Eurasia, encompassing parts of Siberia, southern Russia, and extending southward to the Caspian Sea. These coincide with an exceptionally intense and persistent heat wave in Siberia from January to June 2020 (Gloege et al., 2022; Overland and Wang, 2021). The positive T2m anomalies along the *Siberian pathway* (see Fig. 1) align with previous findings indicating that the Siberian AR was associated with the transport of considerable heat into higher latitudes (Dada et al., 2022; Kirbus et al., 2023). The area where the two ARs prevailed for at least 3 days within the Arctic Circle coincides with strong T2m anomalies exceeding 6-9°C. Such strong 7-day mean T2m anomalies are extremely unusual, placing them in the upper 98.6% of the

https://doi.org/10.5194/egusphere-2025-6285
Preprint. Discussion started: 5 January 2026

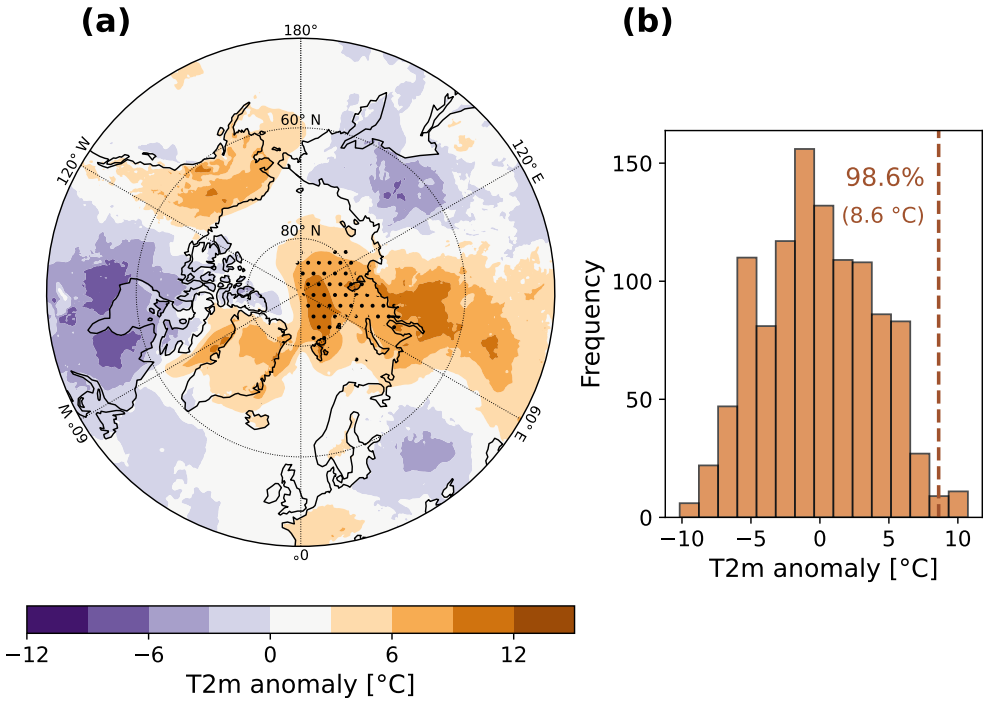

Figure 4. Impact of the Siberian and Atlantic ARs on surface temperature based on ERA5 data. (a) 7-day averaged T2m anomalies for the target period 15-21 April 2020. Stippling highlights areas within the Arctic Circle where AR conditions persisted for at least three days. (b) Distribution of 7-day mean T2m anomalies averaged over the stippling region in (a) for April 1979-2023. The anomaly for the target period is indicated by a vertical line, with the corresponding magnitude and percentile annotated.

climatological distribution for that region (Fig. 4b).

The accumulated precipitation over the target period, expressed relative to the climatological distribution at each grid point (Fig. 5a), reveals extremely unusual precipitation amounts exceeding the 90th percentile along the eastern Greenland coast and across the central Arctic. The latter region coincides with the area where the ARs persisted for at least three days (Fig. 4a). These two regions of extreme precipitation align with the pathways of the two ARs (see Fig. 1), highlighting their role in delivering extremely anomalous precipitation. Based on their respective pathways, the Atlantic AR primarily accounts for the extreme precipitation along the Greenland coast, while both ARs contribute to the exceptionally unusual precipitation over the central Arctic. Further, to assess the impact of both ARs on sea ice, the difference in SIC before and after the event is shown in Fig. 5b. A clear retreat of the sea ice edge is evident along the southeastern Greenland coast and in the Barents-Kara Sea, while an increase in SIC is observed in the Greenland Sea north of Iceland.

https://doi.org/10.5194/egusphere-2025-6285
Preprint. Discussion started: 5 January 2026

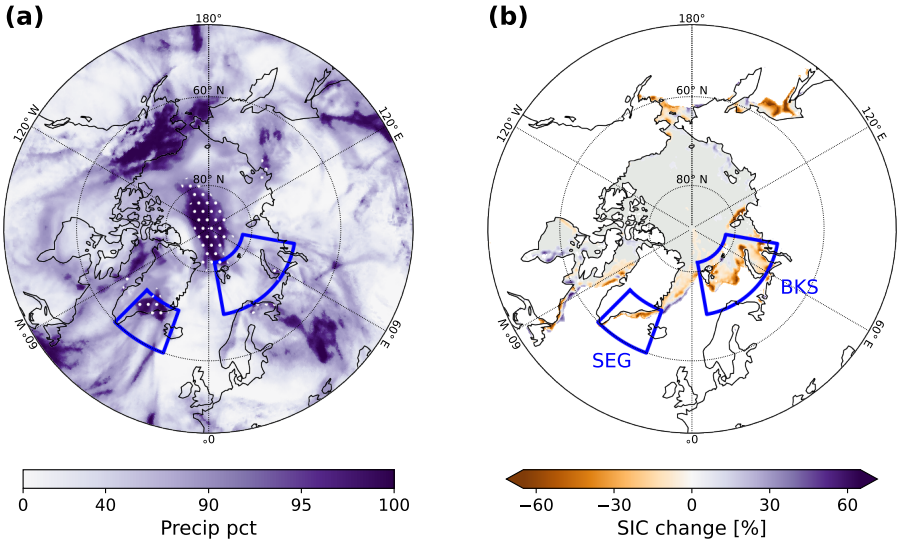

Figure 5. Impact of the Siberian and Atlantic ARs on precipitation and sea ice extent in the Arctic. (a) Percentiles of 7-day gridded accumulated precipitation for the target period relative to the April distribution 1979-2023 based on ERA5. Stippling shows areas within the Arctic Circle where ARs coincide with precipitation $\geq$ 90th percentile. (b) Changes in SIC in the Arctic Ocean between 12 April (before the AR event) and 22 April (after the event) using EUMETSAT OSI SAF OSI-401-b data; grey shading shows sea ice extent. Blue boxes mark the SEG and BKS regions.

To unravel how T2m, precipitation, rainfall and sea ice retreat are interconnected while being impacted by ARs, two boxes are defined along the sea ice edge to capture negative SIC changes (Fig. 5b). One box is defined over south-east Greenland (SEG, 20°-45°W, 60°-70°N) and the other over the Barents-Kara Sea (BKS, 10°-80°E, 70°-82°N); both lie on the pathway of the two ARs. Further, the SEG region encompasses the area along the Greenland coast where highly anomalous precipitation is observed (Fig. 5a), whereas BKS experiences strong and widespread positive T2m anomalies of 6-9°C (Fig. 4a).

Area-averaged time series of T2m, precipitation, rainfall, and SIC are shown in Fig. 6 for the SEG and BKS regions. Over SEG, SIC (Fig. 6a) gradually decreases while T2m undergoes a steady increase throughout April 2020, rising from around –10 °C to slightly above 0 °C by 17 April. Intermittent and well-defined precipitation events are observed in SEG with daily totals exceeding 10 mm day^{-1} (Fig. 6c). In early April, rainfall remains low, whereas later a mix of rain and snow is observed. During the ARs, precipitation rates exceed 10 mm day^{-1} while rainfall surpasses 4 mm day^{-1}. The time series further reveal that notable precipitation and rainfall events also occur outside the period when the ARs are located over SEG. A strong negative correlation is present between SIC and T2m ($r = -0.69$) suggesting that SIC decreases in SEG are closely linked to warmer T2m, whereas the correlation between SIC and precipitation ($r_{\text{precip}} = -0.32$) and between SIC and rainfall ($r_{\text{rain}} = -0.48$) are

https://doi.org/10.5194/egusphere-2025-6285
Preprint. Discussion started: 5 January 2026

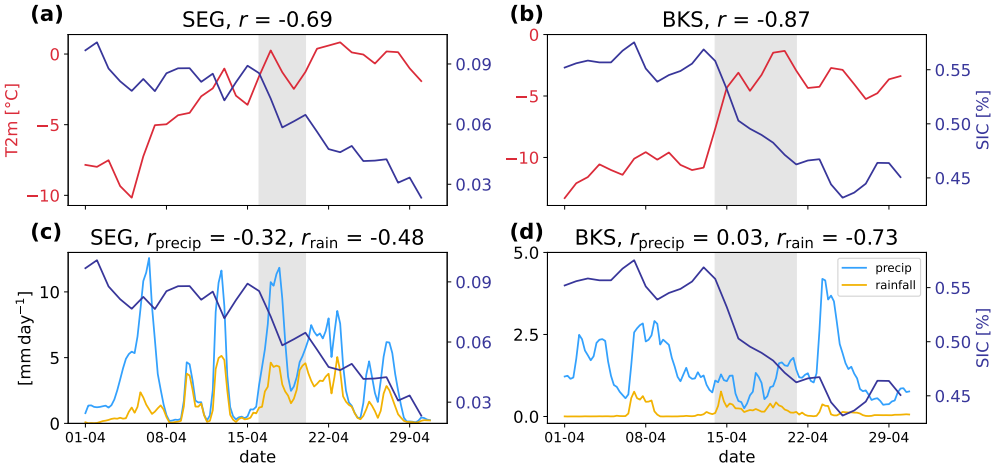

Figure 6. Relation between surface variables and SIC over SEG and BKS based on ERA5 and OSI SAF data for April 2020. (a) Time series of T2m (red) and SIC (blue) averaged over the SEG region. Grey shading indicates the period during which at least one AR is located over the region. The correlation coefficient between the two time series is shown in the panel title. (b) is as in (a), but for the BKS region. (c) and (d) as in (a) and (b) but for SIC, total precipitation (light blue) and rainfall (orange). Here, r_{precip} represents the correlation coefficient between precipitation and SIC in the respective region, while r_{rain} denotes the correlation coefficient between rainfall and SIC.

relatively weak.

Over BKS, SIC (Fig. 6b) undergoes a steady decline throughout April with an accelerated decrease during the ARs. T2m, in contrast, exhibits a sharp increase from -10°C on 12 April, prior to the AR arrival, to 0°C by 18 April. After the AR retreat, T2m drops again to -5°C, possibly due to clear-sky conditions and enhanced radiative cooling. Rainfall in BKS remains generally low (Fig. 6d) due to persistent sub-zero temperatures, although intermittent rainfall events are measured. During the ARs, precipitation increases substantially. A strong negative correlation between T2m and SIC ($r = -0.87$), as well as between rainfall and SIC ($r = -0.73$) indicates that decreases in SIC in the BKS region are closely tied to both surface warming and enhanced rainfall. In contrast, a low correlation is found between total precipitation and SIC.

3.4 Thermodynamic evolution of AR parcels associated with extreme precipitation

Having examined the drivers and surface impacts of the two ARs from a Eulerian point of view, this section uses a Lagrangian framework to analyse the spatial and thermodynamic evolution of airmasses, and the moisture budget along the Siberian and Atlantic pathways. We start by analysing 5-day backward trajectories with endpoints within the Arctic Circle where precipitation exceeds the 90th percentile along the Greenland coast (see white stippling in Fig. 5a). The same analysis is then repeated for trajectories with endpoints in the central Arctic, where highly anomalous precipitation ($\geq$ 90th percentile) is observed dur-

https://doi.org/10.5194/egusphere-2025-6285
Preprint. Discussion started: 5 January 2026

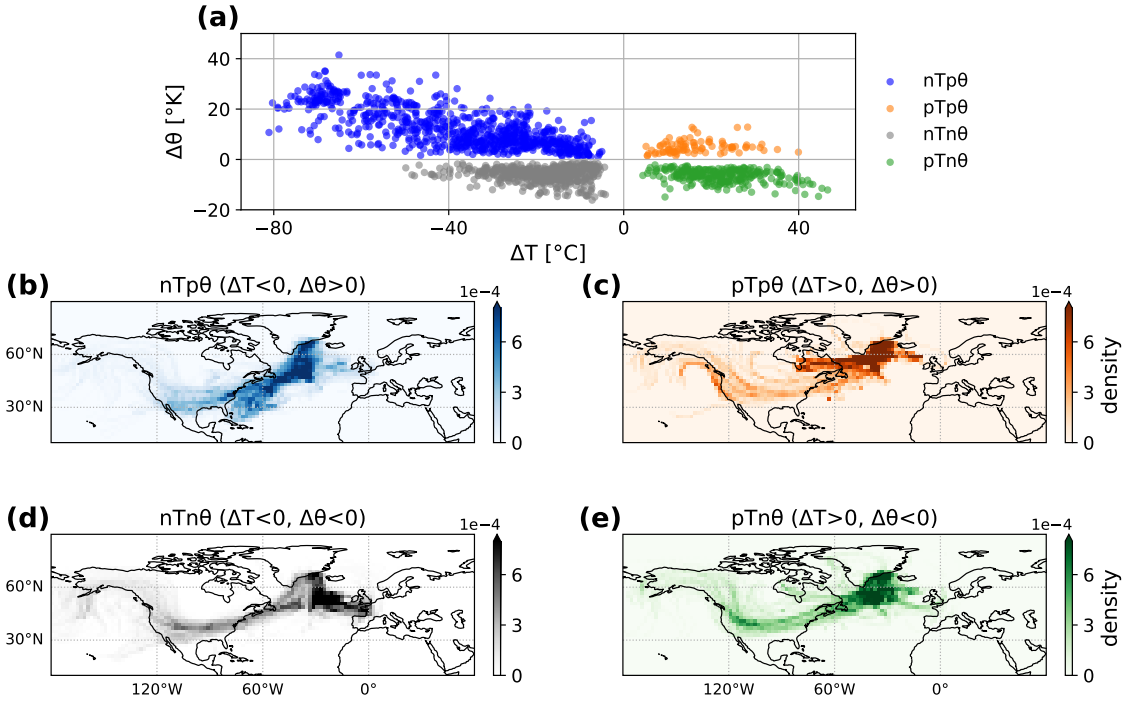

Figure 7. Thermodynamic properties of parcels contributing to extreme precipitation over the Greenland coast within the Arctic Circle (white stippling in Fig. 5a over Greenland). 5-day backward trajectories are considered based on ERA5. (a) Maximum difference in temperature (ΔT) and potential temperature ($\Delta\theta$) along each trajectory relative to their endpoints. Coloured clusters indicate four distinct groups: nTpθ (blue; negative ΔT, positive $\Delta\theta$), pTpθ (orange; positive ΔT, positive $\Delta\theta$), nTnθ (grey; negative ΔT, negative $\Delta\theta$), and pTnθ (green; positive ΔT, negative $\Delta\theta$). (b) Spatial density distribution of nTpθ trajectories. (c) same as (b) but for pTpθ parcels. (d) and (e) same as (b) and (c) but for nTnθ and pTnθ parcels.

ing the two ARs.

Figure 7a shows the scatter plot of the maximum differences in temperature (ΔT) and potential temperature ($\Delta\theta$) relative to their trajectory endpoints, grouping the trajectories into four distinct groups. Positive (negative) ΔT indicate a net temperature increase (decrease), while positive (negative) $\Delta\theta$ reflect diabatic heating (cooling). The nTpθ group (blue, 46.4% of trajectories) experiences cooling, together with diabatic heating. The pTpθ group (orange, 5.3%) undergoes both warming and diabatic heating, while the nTnθ group (grey, 32.4%) shows a net decrease in temperature and diabatic cooling. Finally, the pTnθ group (green, 15.9%) exhibits warming coupled with diabatic cooling.

The spatial density distribution of nTpθ parcels (Fig. 7b) visualises the pathway taken by the corresponding parcels. It reveals that they primarily originate in the mid-latitudes over the western Atlantic, as well as across the USA and subsequently follow

https://doi.org/10.5194/egusphere-2025-6285
Preprint. Discussion started: 5 January 2026

the Atlantic pathway north-eastward along the Gulf Stream before reaching the Greenland coast. This transport pattern agrees with the findings of Waling et al. (2024), who showed that, during summer, ARs reaching Greenland generally originate over the central USA and the western Atlantic between 30° and 45°N. The temporal evolution of key thermodynamic properties averaged across each subgroup (Fig. 8) supports this, indicating that nTpθ parcels typically originate in the mid-latitudes south of 45°N and undergo rapid poleward transport during the final two days before reaching their endpoints (Fig. 8e). The air parcels remain relatively warm (Fig. 8a), averaging near 0°C 3-4 days before arrival, and move at nearly constant potential temperature (Fig. 8b), indicating adiabatic motion. Specific humidity exceeds the surface annual mean of 2.4 $\mathrm{g\,kg^{-1}}$ at 70°N (Serreze et al., 1995) and increases steadily, reaching a maximum 2-3 days prior to arrival (Fig. 8c). The parcels are mainly found around 750 hPa (Fig. 8d), consistent with previous studies showing that the core of an AR and associated strongest horizontal moisture fluxes are concentrated below this level, where air parcels can take up moisture from the surface (Ralph et al., 2017; Guan and Waliser, 2015). The interplay of these thermodynamic variables, their evolution along the trajectories and high moisture content show that nTpθ parcels exhibit characteristics typical for ARs, intensifying over warm ocean waters as they move poleward.

On the last day before landfall, nTpθ parcels experience a sharp decline in temperature and pressure, as well as specific humidity, together with an increase in potential temperature (Fig. 8). This indicates that airmasses rise upon reaching the Greenland coast, leading to cooling, condensation, and precipitation, accompanied by latent heat release. This thermodynamic evolution of nTpθ parcels reflects the complex interplay of surface heat exchange, moisture transport, and vertical mixing typical of ARs as they release moisture upon landfall.

In contrast, the pTpθ, nTnθ and pTnθ groups represent more local transports of airmasses. The nTnθ parcels are primarily located over the north-central Atlantic, west of the UK, with a smaller fraction originating across the USA (Fig. 7d). On average, these parcels follow a northward journey starting around 45°N (Fig. 8e) and are characterised by consistently cold temperatures below -15°C (Fig. 8a). Lower pressure (Fig. 8d) and high potential temperature values (Fig. 8b) indicate that the parcels travel mainly in the middle troposphere. Furthermore, the gradual decline in potential temperature indicates slow diabatic cooling. Specific humidity (Fig. 8c) remains low and nearly constant, suggesting limited moisture uptake or loss. On the final day, the parcels ascend and experience a decline in temperature in addition to decreasing potential temperature. This indicates that nTnθ parcels move from warmer to colder regions and mix with cold airmasses near Greenland, thus, experiencing cooling and energy loss, possibly associated with evaporative processes. Owing to their higher-altitude and cold trajectories, nTnθ parcels are unable to take up moisture along their paths. Thus, despite their spatial proximity, they do not contribute to the extreme precipitation observed along the Greenland coast and lack key characteristics of ARs.

Parcels belonging to the pTpθ and pTnθ groups originate largely over the North Atlantic south of Greenland (Fig. 7c,e) and share similar characteristics. They originate near 60°N and follow a descending pathway from the mid-troposphere towards the lower altitudes (Fig. 8). Along their trajectories, the temperature and specific humidity increase, indicating interactions with the underlying surface. However, both groups remain relatively cold and retain overall low moisture content, limiting their

https://doi.org/10.5194/egusphere-2025-6285
Preprint. Discussion started: 5 January 2026

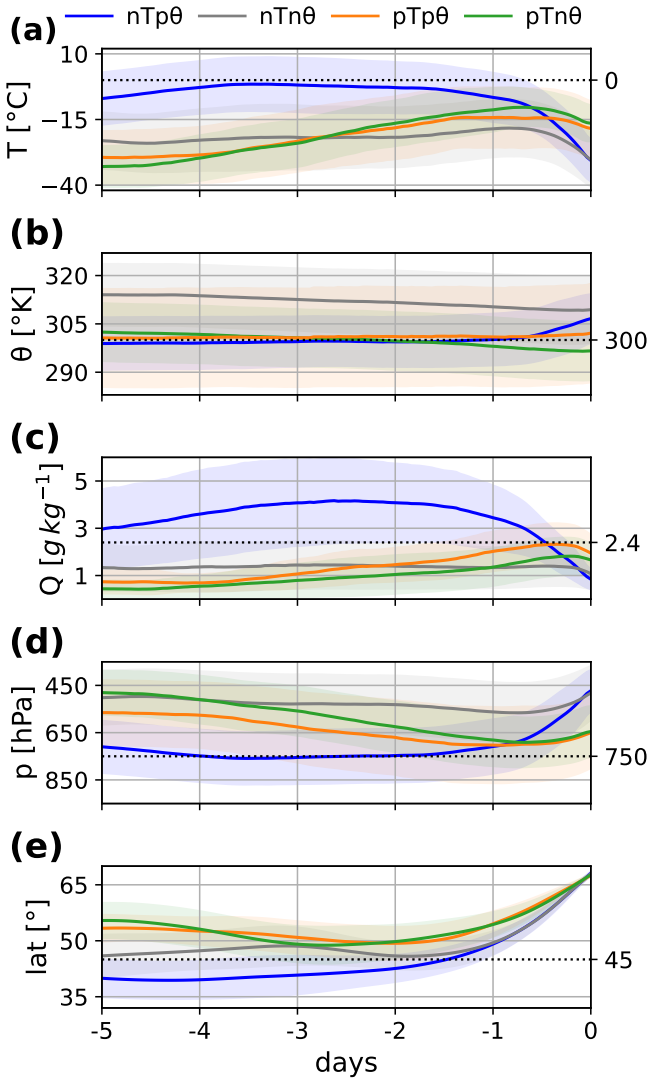

Figure 8. Time evolution of thermodynamic properties along 5-day back trajectories based on ERA5. Panel (a) shows the temporal evolution of temperature averaged over each subgroup from Fig. 7 with the envelopes indicating ± 0.5 s.d. of the spread across the constituent trajectories. The black dotted line marks 0°C. (b) as in (a) but for the potential temperature with the black line marking 300°K, indicating the tropopause in polar regions. (c) as in (a) but for specific humidity; the black dotted line indicates the annual mean surface specific humidity at 70°N. (d) as in (a) but for the pressure evolution; the black line marks 750 hPa. (e) as in (a) but for the mean latitude with the black line marking 45°N.

contribution to precipitation along the Greenland coast.

325

https://doi.org/10.5194/egusphere-2025-6285
Preprint. Discussion started: 5 January 2026

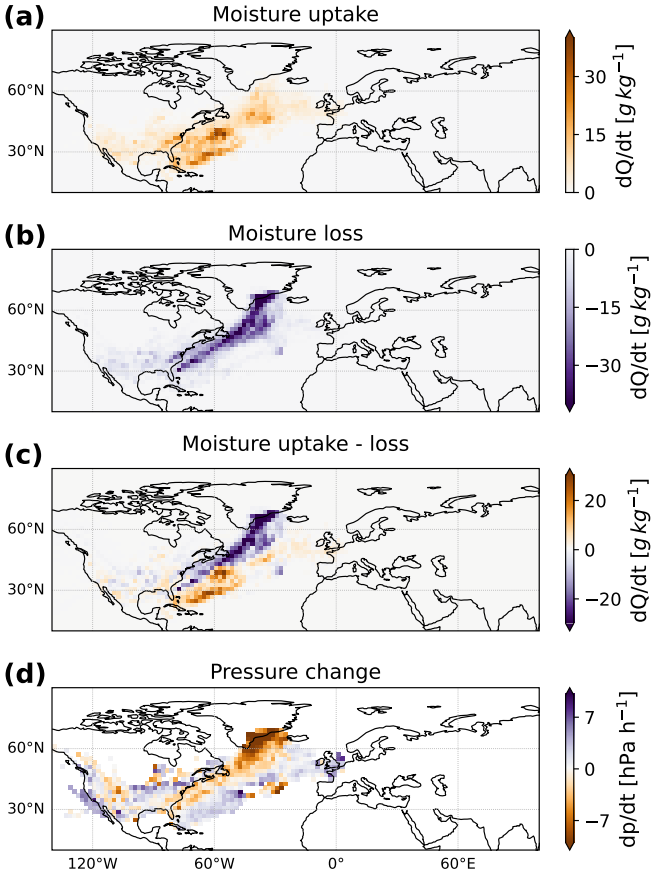

Figure 9. Moisture budget analysis of 5-day back trajectories for parcels belonging to the nTpθ group (see Fig. 7a) based on ERA5. From top to bottom, the panels show: (a) Spatial distribution of accumulated moisture uptake (dQ/dt>0) along the trajectories. (b) Same as for (a) but for moisture loss (dQ/dt <0). (c) Spatial distribution of the net moisture budget, calculated as the difference between panels (b) and (c), i.e. moisture uptake minus loss. (d) Map of average pressure changes per parcel for bins containing more than 20 parcels.

After having determined that nTpθ parcels exhibit key AR characteristics and act as the primary conveyors of extreme precipitation to the Greenland coast, we next focus on moisture uptake and loss regions along their trajectories. Figure 9 reveals that in general moisture uptake occurs predominantly at lower latitudes (Fig. 9a) and in the lower levels of the troposphere near 900 hPa (not shown). In contrast, moisture loss takes place at higher latitudes (Fig. 9b) and in the mid-troposphere (not shown). Further, moisture uptake is most pronounced over the western Atlantic near the USA coast, where warm sea surface temperatures favour upward turbulent surface fluxes, and over the north-central Atlantic south-east of Greenland. In contrast, moisture loss, corresponding to precipitation, is confined to a narrow filament along the Atlantic pathway from the eastern coast of Florida to Greenland. This loss intensifies near the Greenland coast, where orographic uplift of the landfalling Atlantic

https://doi.org/10.5194/egusphere-2025-6285
Preprint. Discussion started: 5 January 2026

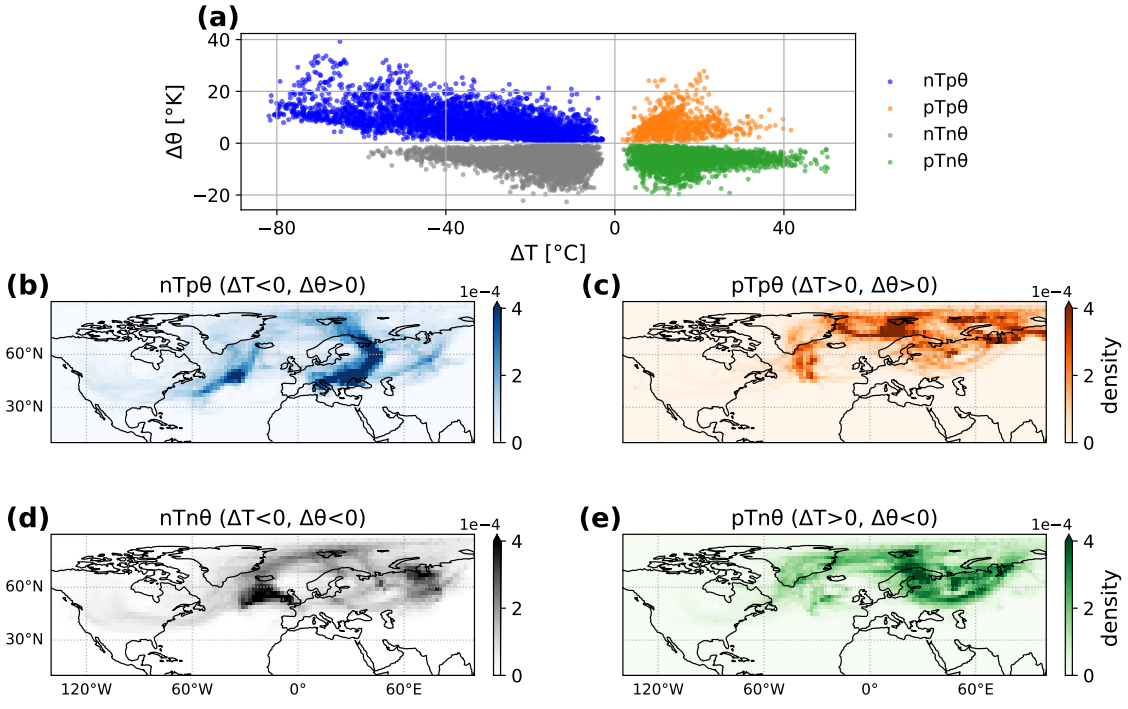

Figure 10. Same as Fig. 7 but for 7-day back trajectories of parcels with endpoints in the central Arctic where precipitation ≥ 90 percentile (see white stippling in Fig. 5a).

AR leads to extreme precipitation, as indicated by a marked decrease in the averaged parcel pressure in this region (Fig. 9d).

Next, the trajectory analysis is repeated for parcels with endpoints in the central Arctic, where extreme precipitation occurred during the two ARs (see white stippling in Fig. 5a). For this region, 7-day parcel trajectories are considered, again yielding four distinct groups based on the maximum changes in ΔT and $\Delta\theta$ along each trajectory relative to its endpoint. Figure 10a shows the resulting groups: nTpθ (26.5% of trajectories), pTpθ (6.1%), nTnθ (47.6%), and pTnθ (19.8%). Compared to the Greenland coast, where nearly half of the parcels fell within nTpθ, the dominant group in the central Arctic is nTnθ, while nTpθ accounts for only about one quarter of the trajectories.

The trajectory density map for the nTpθ group (Fig. 10b) clearly captures the distinct pathways of both the Atlantic and Siberian ARs. Along the Atlantic, an elongated stream is shown, coinciding with regions of enhanced moisture uptake (Fig. 12a) and low parcel altitudes around 900 hPa (not shown). Moisture loss, accompanied by upward motion (Fig. 12b,d), also occurs in the same region but is concentrated further north. Additionally, strong moisture loss and upward motion is shown over the Greenland coast. Over Eurasia, two distinct trajectory pathways emerge. One extends from southeastern Europe through Siberia and eastern Scandinavia, reaching the Arctic Ocean and Svalbard. The other, less pronounced, follows a similar arch-

https://doi.org/10.5194/egusphere-2025-6285
Preprint. Discussion started: 5 January 2026

shaped route farther east over Russia and Siberia, terminating over the Kara Sea. Both pathways are associated with the Siberian AR, where a south-eastward shift of the driving low-high pressure couplet leads to an eastward displacement of the AR track (see Fig. 1). Moisture uptake along the Siberian pathway is most prominent over south-eastern Europe and western Russia, while the eastern route shows limited moisture uptake east of the Urals (Fig. 12a). Moisture loss is concentrated over southern Europe and Russia along an arch-shaped route (Fig. 12b). The close spatial alignment between moisture source and sink regions along the AR pathway suggests that a substantial fraction of the precipitated moisture is being locally recycled within the AR, as has been shown in previous studies (Nusbaumer and Noone, 2018).

The temporal evolution properties along the trajectories show that nTpθ parcels reaching the central Arctic typically originate near 50°N and travel northward, mainly during the final three days before arrival (Fig. 11e). They are characterised by relatively warm temperatures compared to pTpθ, nTnθ and pTnθ parcels (Fig. 11a), although their average temperatures remain below 0°C. Their nearly constant potential temperature indicates adiabatic motion (Fig. 11b), while pressure values around 750 hPa suggest that the parcels travel within the lower troposphere (Fig. 11d). Similar to nTpθ parcels reaching the Greenland coast (see Fig. 8c), those arriving in the central Arctic have high specific humidity (Fig. 11c). However, whereas the Greenland-bound nTpθ parcels exhibit a marked increase in Q along their trajectories, the central Arctic parcels maintain comparatively flat Q values. This indicates that a substantial fraction of the moisture was acquired upstream, more than 7 days before the airmasses reached the central Arctic. A steady decrease in temperature, along with decreasing humidity and increasing pressure 1–3 days before arrival, coincides with the northward propagation of the parcels into the colder Arctic environment, reflecting progressive cooling and ascent, particularly between 60° and 70°N.

Parcels in the nTnθ group primarily originate from the north-central Atlantic and the UK, following an arch-shaped pathway along eastern Greenland into the high latitudes. Additional trajectories are observed over central Siberia and the Kara Sea across northern Eurasia, though at lower densities. These parcels represent a high-altitude feature characterised by low pressure, elevated potential temperature, and low, nearly constant specific humidity (Fig. 11). Given these characteristics, the nTnθ group does not appears to be part of the incoming AR plumes and likely contributes minimally to the anomalous precipitation observed in the central Arctic during the period. In contrast, the pTpθ and pTnθ groups seem to be linked to more localised processes, similar to those observed for the parcels reaching the Greenland coast. Like the nTnθ group, they exhibit low temperatures and low specific humidity, which limit their capacity to produce significant precipitation.

4 Discussion and Conclusion

By utilising a combined Eulerian and Lagrangian analysis framework, we have identified the dynamical drivers, local and Arctic-wide surface impacts, and the thermodynamic evolution of two distinct Arctic ARs during 13-21 April 2020. Together, these ARs contributed to highly unusual atmospheric conditions across the Arctic, underscoring their critical role in amplifying

https://doi.org/10.5194/egusphere-2025-6285
Preprint. Discussion started: 5 January 2026

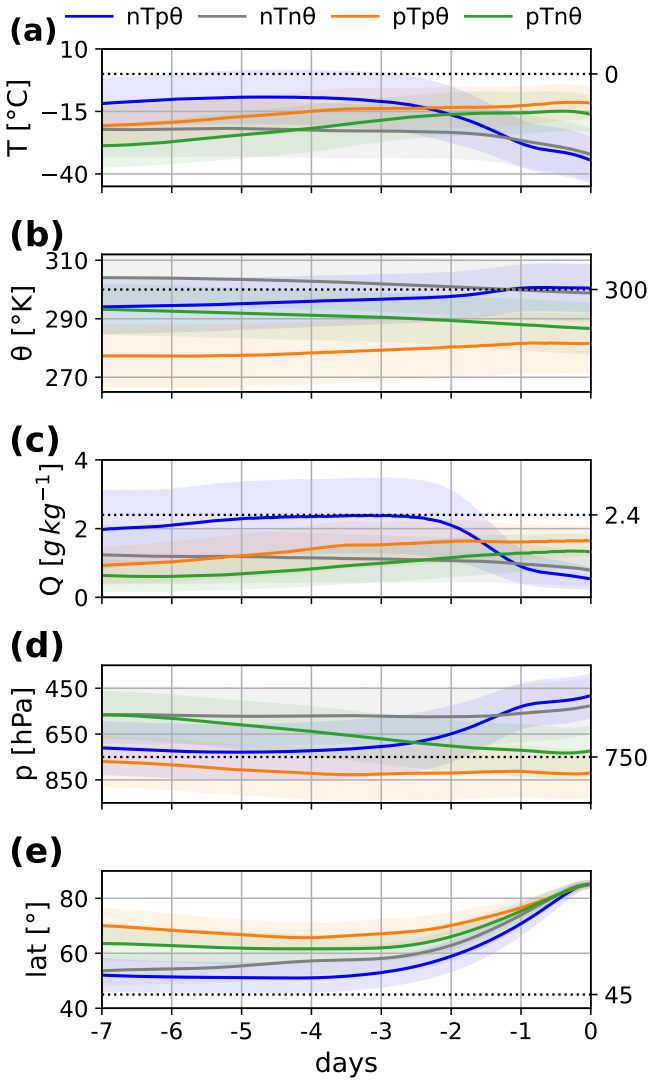

Figure 11. Same as Fig. 8 but for subgroups from Fig 10 and 7-day back trajectories.

https://doi.org/10.5194/egusphere-2025-6285
Preprint. Discussion started: 5 January 2026

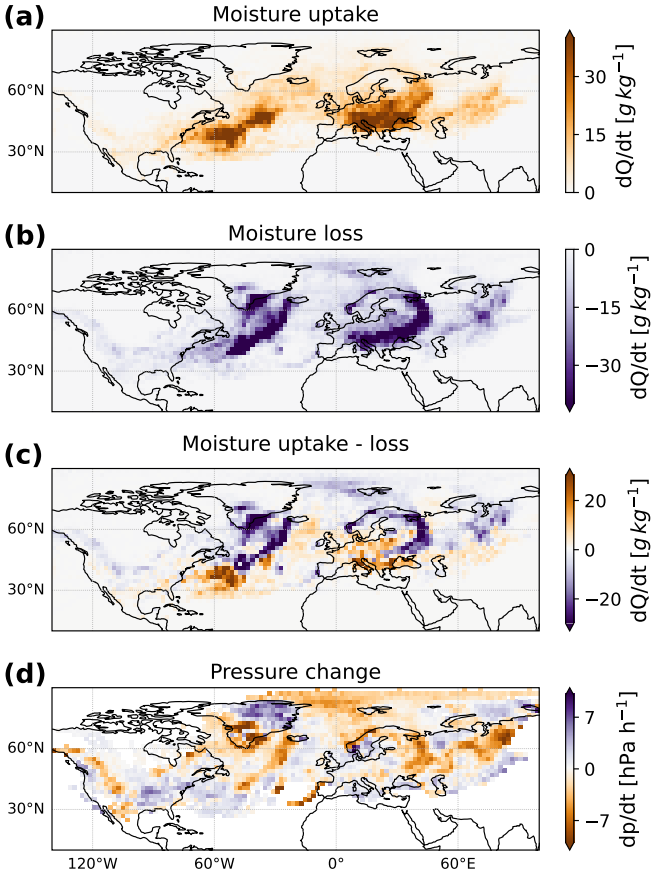

Figure 12. Same as Fig. 9 but for 7-day back trajectories of nTnθ parcels from Fig. 10. For panel (d) only bins with more than 50 parcels are taken into account.

regional weather extremes, and shaping Arctic climate variability and associated cryospheric impacts.

Our analysis captures the detailed temporal evolution of the large-scale circulation patterns that steered the two major ARs into the Arctic (see Fig. 1), resulting in unprecedented transport of heat and moisture into the region. The Atlantic AR was driven by a highly exceptional cyclone over Baffin Bay and an anticyclone over the North Atlantic, while the Siberian AR was driven by a cyclone over western Siberia and an extremely anomalous and persistent anticyclone over north-central Siberia (Fig. 2). The two ARs had distinct characteristics and regional impacts. The Siberian AR was more strongly associated with widespread surface temperature anomalies, particularly across the Eurasian landmass (Fig. 4), while the Atlantic AR was characterised by abundant moisture transport, producing intense precipitation along the Greenland coast (Fig. 5a). The ARs led to increased cloud cover, enhanced downward longwave radiation, and regional warming (Fig. 3 and Fig. 6), coinciding with

https://doi.org/10.5194/egusphere-2025-6285
Preprint. Discussion started: 5 January 2026

notable sea ice retreat in the Barents-Kara Sea and along the south-eastern coast of Greenland (Fig. 5b).

Backward parcel trajectories associated with extreme precipitation along the Greenland coast provide new insights into the thermodynamic evolution of the Atlantic AR. We identify four distinct groups of air parcels, each exhibiting unique thermodynamic characteristics (Fig. 7). Three of these groups are marked by persistently cold temperatures and low specific humidity (Fig. 8). Although embedded within the same synoptic system, these air parcels do not belong to the AR plume. In contrast, the dominant group, comprising roughly half of the trajectories, is primarily responsible for the anomalously high precipitation along the Greenland coast and displays clear AR characteristics (Fig. 8 and Fig. 9). These parcels originate south of 40°N and travel northward along the eastern coast of the USA, drawing moisture predominantly from the warm waters of the Gulf Stream (Fig. 9). The air parcels are characterised by relatively warm temperatures that increase to around 0°C, increased specific humidity, and low pressure during transport. Upon reaching Greenland, they ascend rapidly, cool, and release moisture through intense precipitation accompanied by latent heat release.

Trajectories associated with extreme precipitation in the central Arctic similarly reveal four distinct groups, three of which show limited potential for precipitation (Fig. 10). The remaining group, accounting for roughly one quarter of the trajectories, displays clear signatures of both the Atlantic and Siberian ARs and is characterised by poleward transport of moist, relatively warm air from the midlatitudes (Fig. 11 and Fig. 12). These parcels travel within the lower troposphere under near-adiabatic conditions, gradually cooling and losing moisture as they enter the colder Arctic environment, where precipitation occurs north of 80°N.

The Siberian AR derived its moisture from continental Eurasia (Fig. 12). Previous studies have shown that strong positive T2m anomalies over Siberia in early 2020 led to an unusually early onset of snowmelt, enhanced soil moisture, and earlier greening (Gloege et al., 2022; Kwon et al., 2021). These conditions likely provide a significant moisture reservoir for the Siberian AR. At the same time, regions of moisture uptake and loss along the Siberian AR spatially align,indicating that part of the moisture is locally recycled over Eurasia within the AR (Nusbaumer and Noone, 2018). This implies that a portion of the moisture reaching the central Arctic is not newly acquired over Eurasia, but carried from more distant regions over a period exceeding seven days, highlighting the importance of long-range transport in sustaining the moisture content of the Siberian AR.

Our findings align with previous research on the role of ARs in transporting heat and moisture into polar regions (Gorodetskaya et al., 2014; Wille et al., 2019; Payne et al., 2020; Wang et al., 2024). We complement recent works by Kirbus et al. (2023) and Svensson et al. (2023), who analysed the same event using combined Eulerian and Lagrangian approaches, primarily focusing on impacts in the vicinity of RV *Polarstern*. Kirbus et al. (2023) emphasised the poleward transport of latent energy, associated cloud modifications, and surface energy balance anomalies driven by turbulent heat fluxes and radiation. Svensson et al. (2023), in turn, highlighted the large-scale circulation patterns channelling warm air intrusions into the Arctic,

https://doi.org/10.5194/egusphere-2025-6285
Preprint. Discussion started: 5 January 2026

their surface impacts at the ship's location, and Lagrangian air-mass transformations along three distinct pathways reaching the vessel. By tracing the origin and evolution of air parcels associated with AR-induced extreme Arctic precipitation, our analysis extends previous findings by showing how distinct trajectory groups contributed to the build-up and release of moisture, thereby linking the large-scale transport dynamics directly to the precipitation observed along the Greenland coast and the central Arctic.

In a warming climate, increasing atmospheric moisture content in the Arctic, together with declining sea ice and enhanced storm activity (Iijima et al., 2016), is expected to intensify AR activity and expand their reach into the high latitudes. Recent evidence suggests that Siberian ARs are becoming more frequently occurring features of the Arctic climate system (Komatsu et al., 2018), raising important questions about how the combined transport of heat, moisture, and aerosols influences Arctic amplification and cloud radiative forcing. Continued investigation into the mechanisms, variability, and impacts of ARs under a changing climate will be essential for improving projections and informing climate resilience strategies in the Arctic and beyond.

Data availability. All data used for this study is publicly available. ERA5 reanalysis data is provided by ECMWF and can be accessed at www.ecmwf.int/en/forecasts/dataset/ecmwf-reanalysis-v5 (last accessed 01/09/2025). MOSAiC meteorological data is available from the Arctic Data Centre at doi.org/10.18739/A2PV6B83F, and MOSAiC precipitation data at doi.org/10.18739/A2WD3Q35Z. The EUMETSAT OSI SAF product OSI-401-b is available at dx.doi.org/10.15770/EUM_SAF_OSI_NRT_2004. We thank Guan and Waliser for making AR category database available at dataverse.ucla.edu/dataverse/ar.

Author contributions. LEAP conducted the analyses of synoptic conditions, AR-precipitation-SIC connections, and in-situ observations guided by HL. LEAP carried out the trajectory calculations, supported by PM, AY, and TP. LEAP wrote the original manuscript. All authors provided input on the interpretation of the results, as well as editing and reviewing the manuscript.

Competing interests. The authors declare that they have no conflict of interest.

Acknowledgements. LEAP is supported by the Natural Environment Research Council (NERC) Satellite Data in Environmental Science (SENSE) Centre for Doctoral Training (NE/T00939X/1). HL and TJB were supported by NERC-CANARI project (NE/W004984/1). AEH is supported by ESA through the 5D Antarctica project (4000146702/24/I-KE). ACM is supported by the NERC-ExtAnt project (NE/Y503307/1). This work also benefited from funding provided by the UK–Japan Arctic Research Bursary Scheme.

https://doi.org/10.5194/egusphere-2025-6285
Preprint. Discussion started: 5 January 2026

References

Binder, H., Boettcher, M., Grams, C. M., Joos, H., Pfahl, S., and Wernli, H.: Exceptional Air Mass Transport and Dynamical Drivers of an Extreme Wintertime Arctic Warm Event, Geophysical Research Letters, 44, 028–12, https://doi.org/10.1002/2017GL075841, 2017.

Bintanja, R. and Selten, F. M.: Future increases in Arctic precipitation linked to local evaporation and sea-ice retreat, Nature, 509, 479–482, https://doi.org/10.1038/nature13259, 2014.

Boisvert, L. N., Petty, A. A., and Stroeve, J. C.: The Impact of the Extreme Winter 2015/16 Arctic Cyclone on the Barents–Kara Seas, Monthly Weather Review, 144, 4279–4287, https://doi.org/10.1175/MWR-D-16-0234.1, 2016.

Bonne, J. L., Steen-Larsen, H. C., Risi, C., Werner, M., Sodemann, H., Lacour, J. L., Fettweis, X., Cesana, G., Delmotte, M., Cattani, O., Vallelonga, P., Kjær, H. A., Clerbaux, C., Sveinbjörnsdóttir, Á. E., and Masson-Delmotte, V.: The summer 2012 Greenland heat wave: In situ and remote sensing observations of water vapor isotopic composition during an atmospheric river event, Journal of Geophysical Research, 120, 2970–2989, https://doi.org/10.1002/2014JD022602, 2015.

Box, J. E., Wehrlé, A., van As, D., Fausto, R. S., Kjeldsen, K. K., Dachauer, A., Ahlstrøm, A. P., and Picard, G.: Greenland Ice Sheet Rainfall, Heat and Albedo Feedback Impacts From the Mid-August 2021 Atmospheric River, Geophysical Research Letters, 49, https://doi.org/10.1029/2021GL097356, 2022.

Cox, C. J., Gallagher, M. R., Shupe, M. D., Persson, P. O. G., Solomon, A., Fairall, C. W., Ayers, T., Blomquist, B., Brooks, I. M., Costa, D., Grachev, A., Gottas, D., Hutchings, J. K., Kutchenreiter, M., Leach, J., Morris, S. M., Morris, V., Osborn, J., Pezoa, S., Preußer, A., Riihimaki, L. D., and Uttal, T.: Continuous observations of the surface energy budget and meteorology over the Arctic sea ice during MOSAiC, Scientific Data, 10, https://doi.org/10.1038/s41597-023-02415-5, 2023.

Cullather, R. I., Lim, Y. K., Boisvert, L. N., Brucker, L., Lee, J. N., and Nowicki, S. M.: Analysis of the warmest Arctic winter, 2015–2016, Geophysical Research Letters, 43, 808–10, https://doi.org/10.1002/2016GL071228, 2016.

Dacre, H. F., Clark, P. A., Martinez-Alvarado, O., Stringer, M. A., and Lavers, D. A.: How do atmospheric rivers form?, Bulletin of the American Meteorological Society, 96, 1243–1255, https://doi.org/10.1175/BAMS-D-14-00031.1, 2015.

Dada, L., Angot, H., Beck, I., Baccarini, A., Quéléver, L. L., Boyer, M., Laurila, T., Brasseur, Z., Jozef, G., de Boer, G., Shupe, M. D., Henning, S., Bucci, S., Dütsch, M., Stohl, A., Petäjä, T., Daellenbach, K. R., Jokinen, T., and Schmale, J.: A central arctic extreme aerosol event triggered by a warm air-mass intrusion, Nature Communications, 13, https://doi.org/10.1038/s41467-022-32872-2, 2022.

Doyle, J. G., Lesins, G., Thackray, C. P., Perro, C., Nott, G. J., Duck, T. J., Damoah, R., and Drummond, J. R.: Water vapor intrusions into the High Arctic during winter, Geophysical Research Letters, 38, https://doi.org/10.1029/2011GL047493, 2011.

Gloege, L., Kornhuber, K., Skulovich, O., Pal, I., Zhou, S., Ciais, P., and Gentine, P.: Land-Atmosphere Cascade Fueled the 2020 Siberian Heatwave, AGU Advances, 3, https://doi.org/10.1029/2021AV000619, 2022.

Gong, Z., Zhong, L., Hua, L., and Feng, J.: Dynamic and Thermodynamic Impacts of Atmospheric Rivers on Sea Ice Thickness in the Arctic since 2000, Journal of Climate, 38, 2873–2890, https://doi.org/10.1175/JCLI-D-23-0509.1, 2025.

Gorodetskaya, I. V., Tsukernik, M., Claes, K., Ralph, M. F., Neff, W. D., and Van Lipzig, N. P.: The role of atmospheric rivers in anomalous snow accumulation in East Antarctica, Geophysical Research Letters, 41, 6199–6206, https://doi.org/10.1002/2014GL060881, 2014.

Graversen, R. G., Mauritsen, T., Drijfhout, S., Tjernström, M., and Mårtensson, S.: Warm winds from the Pacific caused extensive Arctic sea-ice melt in summer 2007, Climate Dynamics, 36, 2103–2112, https://doi.org/10.1007/s00382-010-0809-z, 2011.

Guan, B. and Waliser, D. E.: Detection of atmospheric rivers: Evaluation and application of an algorithm for global studies, Journal of Geophysical Research, 120, 514–12, https://doi.org/10.1002/2015JD024257, 2015.

https://doi.org/10.5194/egusphere-2025-6285
Preprint. Discussion started: 5 January 2026

Guan, B. and Waliser, D. E.: A regionally refined quarter-degree global atmospheric rivers database based on ERA5, Scientific Data, 11, https://doi.org/10.1038/s41597-024-03258-4, 2024.

Hao, M., Luo, Y., Lin, Y., Zhao, Z., Wang, L., and Huang, J.: Contribution of atmospheric moisture transport to winter Arctic warming, International Journal of Climatology, 39, 2697–2710, https://doi.org/10.1002/joc.5982, 2019.

Hegyi, B. M. and Taylor, P. C.: The Unprecedented 2016–2017 Arctic Sea Ice Growth Season: The Crucial Role of Atmospheric Rivers and Longwave Fluxes, Geophysical Research Letters, 45, 5204–5212, https://doi.org/10.1029/2017GL076717, 2018.

Hersbach, H., Bell, B., Berrisford, P., Hirahara, S., Horányi, A., Muñoz-Sabater, J., Nicolas, J., Peubey, C., Radu, R., Schepers, D., Simmons, A., Soci, C., Abdalla, S., Abellan, X., Balsamo, G., Bechtold, P., Biavati, G., Bidlot, J., Bonavita, M., De Chiara, G., Dahlgren, P., Dee, D., Diamantakis, M., Dragani, R., Flemming, J., Forbes, R., Fuentes, M., Geer, A., Haimberger, L., Healy, S., Hogan, R. J., Hólm, E., Janisková, M., Keeley, S., Laloyaux, P., Lopez, P., Lupu, C., Radnoti, G., de Rosnay, P., Rozum, I., Vamborg, F., Villaume, S., and Thépaut, J. N.: The ERA5 global reanalysis, Quarterly Journal of the Royal Meteorological Society, 146, 1999–2049, https://doi.org/10.1002/qj.3803, 2020.

Iijima, Y., Nakamura, T., Park, H., Tachibana, Y., and Fedorov, A. N.: Enhancement of Arctic storm activity in relation to permafrost degradation in eastern Siberia, International Journal of Climatology, 36, 4265–4275, https://doi.org/10.1002/joc.4629, 2016.

Kirbus, B., Tiedeck, S., Camplani, A., Chylik, J., Crewell, S., Dahlke, S., Ebell, K., Gorodetskaya, I., Griesche, H., Handorf, D., Höschel, I., Lauer, M., Neggers, R., Rückert, J., Shupe, M. D., Spreen, G., Walbröl, A., Wendisch, M., and Rinke, A.: Surface impacts and associated mechanisms of a moisture intrusion into the Arctic observed in mid-April 2020 during MOSAiC, Frontiers in Earth Science, 11, https://doi.org/10.3389/feart.2023.1147848, 2023.

Kolbe, M., Bintanja, R., van der Linden, E. C., and Cordero, R. R.: Vertical structure and surface impact of atmospheric rivers reaching antarctic sea ice and land, Atmospheric Research, 315, https://doi.org/10.1016/j.atmosres.2024.107841, 2025.

Komatsu, K. K., Alexeev, V. A., Repina, I. A., and Tachibana, Y.: Poleward upgliding Siberian atmospheric rivers over sea ice heat up Arctic upper air, Scientific Reports, 8, https://doi.org/10.1038/s41598-018-21159-6, 2018.

Kwon, M. J., Ballantyne, A., Ciais, P., Bastos, A., Chevallier, F., Liu, Z., Green, J. K., Qiu, C., and Kimball, J. S.: Siberian 2020 heatwave increased spring CO2uptake but not annual CO2uptake, Environmental Research Letters, 16, https://doi.org/10.1088/1748-9326/ac358b, 2021.

Li, L., Cannon, F., Mazloff, M. R., Subramanian, A. C., Wilson, A. M., and Ralph, F. M.: Impact of atmospheric rivers on Arctic sea ice variations, Cryosphere, 18, 121–137, https://doi.org/10.5194/tc-18-121-2024, 2024.

Liu, C. and Barnes, E. A.: Extrememoisture transport into the Arctic linked to Rossby wave breaking, Journal of Geophysical Research, 120, 3774–3788, https://doi.org/10.1002/2014JD022796, 2015.

Loeb, N. A., Crawford, A., Herrington, A., McCrystall, M., Stroeve, J., and Hanesiak, J.: Projections and Physical Drivers of Extreme Precipitation in Greenland & Baffin Bay, Journal of Geophysical Research: Atmospheres, 129, https://doi.org/10.1029/2024JD041375, 2024.

Mattingly, K. S., Mote, T. L., and Fettweis, X.: Atmospheric River Impacts on Greenland Ice Sheet Surface Mass Balance, Journal of Geophysical Research: Atmospheres, 123, 8538–8560, https://doi.org/10.1029/2018JD028714, 2018.

Mattingly, K. S., Turton, J. V., Wille, J. D., Noël, B., Fettweis, X., Rennermalm, Å. K., and Mote, T. L.: Increasing extreme melt in northeast Greenland linked to foehn winds and atmospheric rivers, Nature Communications, 14, 1743, https://doi.org/10.1038/s41467-023-37434-8, 2023.

https://doi.org/10.5194/egusphere-2025-6285
Preprint. Discussion started: 5 January 2026

Nash, D., Waliser, D., Guan, B., Ye, H., and Ralph, F. M.: The Role of Atmospheric Rivers in Extratropical and Polar Hydroclimate, Journal of Geophysical Research: Atmospheres, 123, 6804–6821, https://doi.org/10.1029/2017JD028130, 2018.

Neff, W.: Atmospheric rivers melt Greenland, Nature Climate Change, 8, 857–858, https://doi.org/10.1038/s41558-018-0297-4, 2018.

Nicolaus, M., Perovich, D. K., Spreen, G., Granskog, M. A., von Albedyll, L., Angelopoulos, M., Anhaus, P., Arndt, S., Jakob Belter, H., Bessonov, V., Birnbaum, G., Brauchle, J., Calmer, R., Cardellach, E., Cheng, B., Clemens-Sewall, D., Dadic, R., Damm, E., de Boer, G., Demir, O., Dethloff, K., Divine, D. V., Fong, A. A., Fons, S., Frey, M. M., Fuchs, N., Gabarró, C., Gerland, S., Goessling, H. F., Gradinger, R., Haapala, J., Haas, C., Hamilton, J., Hannula, H. R., Hendricks, S., Herber, A., Heuzé, C., Hoppmann, M., Høyland, K. V., Huntemann, M., Hutchings, J. K., Hwang, B., Itkin, P., Jacobi, H. W., Jaggi, M., Jutila, A., Kaleschke, L., Katlein, C., Kolabutin, N., Krampe, D., Kristensen, S. S., Krumpen, T., Kurtz, N., Lampert, A., Lange, B. A., Lei, R., Light, B., Linhardt, F., Liston, G. E., Loose, B., Macfarlane, A. R., Mahmud, M., Matero, I. O., Maus, S., Morgenstern, A., Naderpour, R., Nandan, V., Niubom, A., Oggier, M., Oppelt, N., Pätzold, F., Perron, C., Petrovsky, T., Pirazzini, R., Polashenski, C., Rabe, B., Raphael, I. A., Regnery, J., Rex, M., Ricker, R., Riemann-Campe, K., Rinke, A., Rohde, J., Salganik, E., Scharien, R. K., Schiller, M., Schneebeli, M., Semmling, M., Shimanchuk, E., Shupe, M. D., Smith, M. M., Smolyanitsky, V., Sokolov, V., Stanton, T., Stroeve, J., Thielke, L., Timofeeva, A., Tonboe, R. T., Tavri, A., Tsamados, M., Wagner, D. N., Watkins, D., Webster, M., and Wendisch, M.: Overview of the MOSAiC expedition: Snow and sea ice, Elementa, 10, https://doi.org/10.1525/elementa.2021.000046, 2022.

Nusbaumer, J. and Noone, D.: Numerical Evaluation of the Modern and Future Origins of Atmospheric River Moisture Over the West Coast of the United States, Journal of Geophysical Research: Atmospheres, 123, 6423–6442, https://doi.org/10.1029/2017JD028081, 2018.

Overland, J. E. and Wang, M.: The 2020 Siberian heat wave, International Journal of Climatology, 41, E2341–E2346, https://doi.org/10.1002/joc.6850, 2021.

Pan, M., Lu, M., and Lall, U.: Diversity of cross-pacific atmospheric river main routes, Communications Earth and Environment, 5, https://doi.org/10.1038/s43247-024-01552-y, 2024.

Papritz, L., Hauswirth, D., and Hartmuth, K.: Moisture origin, transport pathways, and driving processes of intense wintertime moisture transport into the Arctic, Weather and Climate Dynamics, 3, 1–20, https://doi.org/10.5194/wcd-3-1-2022, 2022.

Payne, A. E., Demory, M. E., Leung, L. R., Ramos, A. M., Shields, C. A., Rutz, J. J., Siler, N., Villarini, G., Hall, A., and Ralph, F. M.: Responses and impacts of atmospheric rivers to climate change, https://doi.org/10.1038/s43017-020-0030-5, 2020.

Previdi, M., Smith, K. L., and Polvani, L. M.: Arctic amplification of climate change: A review of underlying mechanisms, https://doi.org/10.1088/1748-9326/ac1c29, 2021.

Ralph, F. M., Iacobellis, S. F., Neiman, P. J., Cordeira, J. M., Spackman, J. R., Waliser, D. E., Wick, G. A., White, A. B., and Fairall, C.: Dropsonde observations of total integrated water vapor transport within North Pacific atmospheric rivers, Journal of Hydrometeorology, 18, 2577–2596, https://doi.org/10.1175/JHM-D-17-0036.1, 2017.

Rinke, A., Cassano, J. J., Cassano, E. N., Jaiser, R., and Handorf, D.: Meteorological conditions during the MOSAiC expedition: Normal or anomalous?, Elementa, 9, https://doi.org/10.1525/elementa.2021.00023, 2021.

Salimi, S., Helali, J., Lotfi, M., Momenzadeh, H., Hosseini, S. A., Asaadi Oskuei, E., Izadi, A., Yarmoradi, Z., and Bakhshi, I.: Investigating the origin and pathways of atmospheric rivers in the world, Theoretical and Applied Climatology, 142, 165–175, https://doi.org/10.1007/s00704-020-03299-w, 2020.

Serreze, M. C. and Barry, R. G.: Processes and impacts of Arctic amplification: A research synthesis, Global and Planetary Change, 77, 85–96, https://doi.org/10.1016/j.gloplacha.2011.03.004, 2011.

https://doi.org/10.5194/egusphere-2025-6285
Preprint. Discussion started: 5 January 2026

Serreze, M. C., Barry, R. G., and Walsh, J. E.: Atmospheric Water Vapor Characteristics at 70°N, Journal of Climate, 8, 719–731, https://doi.org/10.1175/1520-0442(1995)008<0719:AWVCA>2.0.CO;2, 1995.

Shupe, M. D., Rex, M., Dethloff, K., Damm, E., Fong, A. A., Gradinger, R., Heuzé, C., Loose, B., Makarov, A., Maslowski, W., Nicolaus, M., Perovich, D., Rabe, B., Rinke, A., Sokolov, V., and Sommerfeld, A.: Arctic Report Card 2020: The MOSAiC Expedition: A Year Drifting with the Arctic Sea Ice, https://doi.org/https://doi.org/10.25923/9g3v-xh92, 2020.

Shupe, M. D., Rex, M., Blomquist, B., G. Persson, P. O., Schmale, J., Uttal, T., Althausen, D., Angot, H., Archer, S., Bariteau, L., Beck, I., Bilberry, J., Bucci, S., Buck, C., Boyer, M., Brasseur, Z., Brooks, I. M., Calmer, R., Cassano, J., Castro, V., Chu, D., Costa, D., Cox, C. J., Creamean, J., Crewell, S., Dahlke, S., Damm, E., de Boer, G., Deckelmann, H., Dethloff, K., Dütsch, M., Ebell, K., Ehrlich, A., Ellis, J., Engelmann, R., Fong, A. A., Frey, M. M., Gallagher, M. R., Ganzeveld, L., Gradinger, R., Graeser, J., Greenamyer, V., Griesche, H., Griffiths, S., Hamilton, J., Heinemann, G., Helmig, D., Herber, A., Heuzé, C., Hofer, J., Houchens, T., Howard, D., Inoue, J., Jacobi, H. W., Jaiser, R., Jokinen, T., Jourdan, O., Jozef, G., King, W., Kirchgaessner, A., Klingebiel, M., Krassovski, M., Krumpen, T., Lampert, A., Landing, W., Laurila, T., Lawrence, D., Lonardi, M., Loose, B., Lüpkes, C., Maahn, M., Macke, A., Maslowski, W., Marsay, C., Maturilli, M., Mech, M., Morris, S., Moser, M., Nicolaus, M., Ortega, P., Osborn, J., Pätzold, F., Perovich, D. K., Petäjä, T., Pilz, C., Pirazzini, R., Posman, K., Powers, H., Pratt, K. A., Preußer, A., Quéléver, L., Radenz, M., Rabe, B., Rinke, A., Sachs, T., Schulz, A., Siebert, H., Silva, T., Solomon, A., Sommerfeld, A., Spreen, G., Stephens, M., Stohl, A., Svensson, G., Uin, J., Viegas, J., Voigt, C., von der Gathen, P., Wehner, B., Welker, J. M., Wendisch, M., Werner, M., Xie, Z. Q., and Yue, F.: Overview of the MOSAiC expedition- Atmosphere, https://doi.org/10.1525/elementa.2021.00060, 2022.

Sprenger, M. and Wernli, H.: The LAGRANTO Lagrangian analysis tool - Version 2.0, Geoscientific Model Development, 8, 2569–2586, https://doi.org/10.5194/gmd-8-2569-2015, 2015.

Svensson, G., Murto, S., Shupe, M. D., Pithan, F., Magnusson, L., Day, J. J., Doyle, J. D., Renfrew, I. A., Spengler, T., and Vihma, T.: Warm air intrusions reaching the MOSAiC expedition in April 2020- The YOPP targeted observing period (TOP), Elementa, 11, https://doi.org/10.1525/elementa.2023.00016, 2023.

Thaker, R., Vavrus, S. J., Shields, C. A., DuVivier, A. K., Maclennan, M., Holland, M. M., and Landrum, L.: Arctic Atmospheric Rivers in a Changing Climate and the Impacts on Sea Ice, Journal of Geophysical Research: Atmospheres, 130, https://doi.org/10.1029/2024JD042521, 2025.

Tiedeck, S. and Rinke, A.: Extending the Surface Energy Budget View on Arctic Atmospheric Rivers: Climatological Classifications and Dependence on the Flavor, Geophysical Research Letters, 52, https://doi.org/10.1029/2025GL118799, 2025.

Tonboe, R. and Lavelle, J.: The EUMETSAT OSI SAF Sea Ice Concentration Algorithm Algorithm Theoretical Basis Document Documentation Change Record, Tech. rep., The Ocean and Sea Ice Satellite Application Facility, https://osisaf-hl.met.no/sites/osisaf-hl.met.no/files/baseline_document/osisaf_cdop2_ss2_atbd_amsr2-sea-ice-conc_v1p1.pdf, 2016.

Waling, A., Herrington, A., Duderstadt, K., Dibb, J., and Burakowski, E.: Using variable-resolution grids to model precipitation from atmospheric rivers around the Greenland ice sheet, Weather and Climate Dynamics, 5, 1117–1135, https://doi.org/10.5194/wcd-5-1117-2024, 2024.

Wang, Z., Ding, Q., Wu, R., Ballinger, T. J., Guan, B., Bozkurt, D., Nash, D., Baxter, I., Topál, D., Li, Z., Huang, G., Chen, W., Chen, S., Cao, X., and Chen, Z.: Role of atmospheric rivers in shaping long term Arctic moisture variability, Nature Communications, 15, 5505, https://doi.org/10.1038/s41467-024-49857-y, 2024.

Wille, J. D., Favier, V., Dufour, A., Gorodetskaya, I. V., Turner, J., Agosta, C., and Codron, F.: West Antarctic surface melt triggered by atmospheric rivers, Nature Geoscience, 12, 911–916, https://doi.org/10.1038/s41561-019-0460-1, 2019.

https://doi.org/10.5194/egusphere-2025-6285
Preprint. Discussion started: 5 January 2026

Zhang, P., Chen, G., Ting, M., Ruby Leung, L., Guan, B., and Li, L.: More frequent atmospheric rivers slow the seasonal recovery of Arctic sea ice, Nature Climate Change, 13, 266–273, https://doi.org/10.1038/s41558-023-01599-3, 2023.

Zhang, P., Taylor, P. C., Webster, M., Bailey, D. A., Ding, Q., and Li, L.: Unraveling Arctic Sea Ice Response to Atmospheric Rivers—Insights From Sea Ice Modeling, Geophysical Research Letters, 52, https://doi.org/10.1029/2025GL115152, 2025.

Zhu, Y. and Newell, R. E.: A Proposed Algorithm for Moisture Fluxes from Atmospheric Rivers, Monthly Weather Review, 126, 725–735, https://doi.org/10.1175/1520-0493(1998)126<0725:APAFMF>2.0.CO;2, 1998.